Ab Initio Molecular Dynamics Simulation of Divalent Metal Cation Incorporation in Calcite: Implications for Interpreting X-Ray Absorption Spectroscopy Data

Sebastien N. Kerisit[*] *and Micah P. Prange*

Physical and Computational Sciences Directorate, Pacific Northwest National Laboratory, Richland, Washington 99352, United States

October 15th, 2019

ABSTRACT

Calcite ($CaCO_3$) is a ubiquitous mineral with the ability to accommodate a wide range of impurities. Determination of the coordination environment and incorporation modes of impurities in calcite has historically relied primarily on the interpretation of extended X-ray absorption fine structure (EXAFS) spectroscopy. However, a lack of standards combined with the large number of degrees of freedom involved in shell-by-shell fits have made the interpretation of EXAFS spectra challenging. In this work, ab initio molecular dynamics (AIMD) simulations were performed to investigate the incorporation of seven divalent metal cation impurities, namely Ba^{2+}, Pb^{2+}, Sr^{2+}, Cd^{2+}, Mn^{2+}, Co^{2+}, and Zn^{2+}, in calcite. These cations span a wide range of sizes: 30.7% to −22.8% change in ionic radius with respect to Ca^{2+}. The atomic trajectories were then used to compute EXAFS spectra for direct comparison with published experimental spectra. The simulations confirmed that all seven metal cations incorporate in calcite via substitution in the calcium site. The AIMD-EXAFS approach allowed for overcoming limitations of the shell-by-shell fitting approach, such as the difficulties in resolving weak backscatterers beyond the first coordination shell. As a result, the AIMD-EXAFS approach was able to provide a detailed and comprehensive characterization of the structural relaxation around divalent metal cation impurities in calcite.

Keywords: calcium carbonate, ab initio molecular dynamics; extended X-ray absorption fine structure spectroscopy; iso-valent substitution; impurity incorporation; structural relaxation.

INTRODUCTION

Carbonate minerals are abundant at the Earth's surface and are of great importance to global issues such as the carbon cycle and geological carbon sequestration. The carbonate family of minerals also has a significant impact on the chemistry of natural waters and controls the concentration of some metal ions.[1] Calcium carbonate is the most abundant carbonate in sedimentary rocks and is a predominant form of inorganic carbon in the biosphere. Calcite ($CaCO_3$) is the most stable polymorph of calcium carbonate. One of the key properties of calcite is its ability to accommodate a broad range of impurities with varied ionic radii, valences, and molecular symmetries. Impurities known to incorporate in calcite include divalent metal cations,[2] rare-earth elements,[3, 4] actinides,[5-8] and oxyanions.[9-11] Incorporation in calcite of minor and trace elements is crucial to understanding and predicting the mobility, fate, and bioavailability of contaminants and toxic species in near-surface environments. Trace elements incorporated in calcite can also serve as proxies for the evolution of oceans and climate.

A primary experimental technique used to determine the coordination environment, and thus incorporation modes, of impurities is extended X-ray absorption fine structure spectroscopy (EXAFS). In cases such as impurity incorporation where experimental standards are not available, information on the coordination environment of impurities is generally obtained through fitting of the EXAFS signal as shells around the absorbing atom are added, an approach referred to as shell-by-shell fitting. Each coordination shell is defined by its coordination number (CN), absorber-backscatterer distance (R), and Debye-Waller factor (σ^2) and contributes to the normalized EXAFS spectrum,[12] which is defined as

$$\chi(k) = \sum_R \frac{S_0^2 CN}{kR^2} |f(k)| e^{-2R/\lambda(k)} e^{-2\sigma^2 k^2} \times \sin\left(2kR + \Phi(k)\right) \quad \text{Eq. 1}$$

where S_0^2 is the overall amplitude factor and k, $f(k)$, $\lambda(k)$, and $\Phi(k)$ are the photoelectron wavenumber, backscattering amplitude, inelastic mean free path, and backscattering phase. As a result, although constraints are often included, a limitation of this approach is the significant number of degrees of freedom involved in the fits, which can therefore yield non-unique solutions. Additionally, Debye-Waller factors are often used to account for both configurational and thermal disorder, thus providing only an average picture of the multiple coordination environments an impurity may be present in.

An alternative approach is to compute EXAFS spectra from atomic trajectories generated by classical (CMD)[13-16] or ab initio molecular dynamics (AIMD)[17-20] simulations, and subsequently use the calculated spectra as standards in linear combination fits to the experimental data. This approach has the advantage of imposing realistic and systematic constraints on the fits, and thus enables more robust and in-depth data interpretation. For example, when applied to the incorporation of uranium in iron (oxyhydr)oxides,[21-23] this approach allowed for identifying U oxidation states and associated charge compensation schemes, distinguishing between adsorbed and incorporated U, and resolving the preferential incorporation of U in the minor phase of a multiphase system . In this work, this approach is applied to the incorporation of divalent metal cations in calcite. The simulations employ density functional theory (DFT), which has proved to be a powerful theory to describe the structure of calcium carbonate polymorphs[24, 25] and the incorporation of impurities in calcite.[26-34]

EXAFS studies of the incorporation of divalent metal cations in calcite first emerged in the 1990's with seminal work by Pingitore et al.[35] and Reeder and co-workers[2, 36] on Sr^{2+}, Co^{2+}, Zn^{2+}, Pb^{2+}, and Ba^{2+} incorporation in synthetic and natural calcites. Later work in the early 2000's[37, 38] extended this list to include Cu^{2+} and Mn^{2+}. Although outside of the scope of this work, it is worth

noting that EXAFS has been employed to investigate not only bulk incorporation but also surface adsorption of divalent cations at calcite surfaces.[38-42] In several instances, the limitations of the shell-by-shell fitting approach employed in these studies led to inconclusive results and unsolved questions. For example, the large uncertainties on CN in shell-by-shell fitting made interpreting the reported first-shell CNs, which varied between 5.6 and 7.1,[2, 38] difficult. Are some divalent cations truly able to increase their coordination number with respect to the octahedral calcium site they are substituting in?

Here, the AIMD-EXAFS approach is applied to the incorporation of seven divalent metal cations (Ba^{2+}, Pb^{2+}, Sr^{2+}, Cd^{2+}, Mn^{2+}, Co^{2+}, and Zn^{2+}) in calcite. These divalent cations represent percentage changes in ionic radius with respect to Ca^{2+} ranging from −22.8% to +30.7%. The corresponding carbonate endmembers are also considered to provide a validation of the application of this approach to metal carbonate systems. The results of this analysis demonstrate that all the divalent cations within the size range considered in this work retain the six-fold coordination of the original calcium site, but that, upon expansion of the lattice around the impurity for the cations larger than Ca^{2+}, the nearest-neighbor carbonate molecules rotate to shorten the distance between distant oxygen atoms and the impurity. This structural relaxation was missed in shell-by-shell fits due to the difficulties in resolving weak backscatterers beyond the first coordination shell. As such, the AIMD-EXAFS approach allows for painting a more accurate picture of the structural relaxation the calcite structure undergoes to accommodate impurities.

COMPUTATIONAL METHODS

Density functional theory calculations. All of the plane-wave DFT calculations were performed with VASP (Vienna Ab-initio Simulation Package)[43-46] using the projector augmented-wave (PAW) approach.[47, 48] The calculations made use of three generalized gradient

approximation (GGA) exchange-correlation (XC) functionals: two semi-local XC functionals due to Perdew, Burke, and Ernzerhof[49, 50] (PBE) and Hammer et al.[51] (revised PBE or RPBE) and one hybrid functional due to Adamo and Barone (PBE0).[52] For the semi-local functionals, the addition of Grimme dispersion corrections[53, 54] was also evaluated. The PAW potentials were obtained from the VASP database for carbon (2), oxygen (2), magnesium (4), calcium (12), manganese (18), iron (18), cobalt (18), nickel (18), zinc (18), strontium (28), cadmium (36), barium (46), and lead (68), with the number of core electrons shown in parentheses. The convergence criterion for the electronic self-consistent calculation was 10^{-5} eV throughout.

Energy minimizations. Constant-pressure energy minimizations (ionic positions, cell volume, and cell shape are allowed to relax) were performed the determine the crystal structure of four carbonates with the aragonite structure, namely, witherite ($BaCO_3$), cerrusite ($PbCO_3$), strontianite ($SrCO_3$), and aragonite ($CaCO_3$), and eight carbonates with the calcite structure, namely, calcite ($CaCO_3$), otavite ($CdCO_3$), rhodochrosite ($MnCO_3$), siderite ($FeCO_3$), smithsonite ($ZnCO_3$), magnesite ($MgCO_3$), sphaerocobaltite ($CoCO_3$), and gaspeite ($NiCO_3$). The convergence of the crystal structure and total energy per stoichiometric unit with respect to the number of irreducible *k*-points and the plane-wave energy cutoff was evaluated using the PBE XC functional for the two carbonate groups using aragonite and calcite (Tables S1 and S2 of the Supporting Information (SI) document). A plane-wave energy cutoff of 650 eV and 3×3×1 or 3×3×2 *k*-point meshes for calcite and aragonite, respectively, were found to be sufficient to obtain converged crystal structures. These parameters were then used in all the energy minimizations. Convergence was reached when the force on any atom was less than 0.01 eV/Å. Spin-polarized calculations were performed throughout for the carbonates containing cations in an open-shell configuration (i.e., Mn^{2+}, Fe^{2+}, Co^{2+}, and Ni^{2+}) and an antiferromagnetic structure with alternating ferromagnetic layers along the

calcite [001] direction was adopted based on experimental results.[55] All the carbonates with the aragonite structure contained closed-shell cations. The lattice parameters obtained for each XC functional are listed and compared to experimental lattice parameters in Tables S3 to S7 of the SI. The resulting root mean square deviations between experimental and calculated lattice parameters are shown in Table 1. As expected, the hybrid functional performed best, but PBE/D3 showed very similar overall results and was therefore selected for the AIMD simulations as the PBE0 functional would be computationally prohibitive.

Table 1. Root mean square deviations of experimental and calculated lattice parameters of carbonates with either the aragonite or the calcite structure per XC functional.

XC functional	Carbonates with aragonite structure	Carbonates with calcite structure
PBE	1.3	1.2
PBE/D3	0.7	0.8
RPBE	3.4	5.1
RPBE/D3	2.2	1.7
PBE0	0.6	0.3

Ab initio molecular dynamics simulations. The AIMD simulations were performed in the NVT (constant number of particles, constant volume, and constant temperature) ensemble at liquid nitrogen (77 K, LNT) and room (298.15 K, RT) temperatures to match the temperatures of the EXAFS measurements in the literature. The simulations employed the Nosé-Hoover thermostat.[56] For each divalent cation, M^{2+}, for which published EXAFS data was available for the bulk carbonate (MCO_3) and for the divalent cation incorporated in calcite (M^{2+} in $CaCO_3$) for at least one of the two temperatures (M = Ba, Pb, Sr, Cd, Mn, Co, and Zn), AIMD simulations were performed, at the two temperatures, for a 2×2×1 MCO_3 supercell (16 and 24 stoichiometric units for the carbonates with the aragonite and calcite structures, respectively) and for one cation in a

2×2×1 calcite supercell. An integration time step of 0.5 fs was used. The atomic velocities were scaled to the target temperature every 12.5 fs for the first picosecond of the simulation (equilibration), which was not included in subsequent analysis. The simulated time was 7 ps (not including equilibration). The AIMD simulations were performed at the Γ point (1×1×1 *k*-point mesh) with a plane-wave cutoff energy of 600 eV.

EXAFS calculations. A configuration was collected every 50 fs of the 7-ps AIMD simulations to generate a pool of 140 configuration from each AIMD simulation. For each configuration, a cluster with a radius of 8 Å centered on the metal cation of interest was generated to calculate all scattering paths with effective distance less than the cluster radius for a core hole of the central atom using FEFF9.[12, 57, 58] A K core hole was considered for all absorbers, except for Pb for which a L_{III} core hole was considered instead to match the EXAFS measurements in the literature. For the MCO_3 AIMD simulations, a metal cation of the supercell was randomly selected to be the absorber (all carbonates have a single unique crystallographic position of the metal cation), but the same cation was used in each configuration. The S_0^2 parameter calculated by FEFF9 was used in all cases (0.875, 0.937, 0.916, 0.925, 0.935, 0.947, 0.950 for Ba, Pb, Sr, Cd, Mn, Co, and Zn, respectively). For each simulation, the EXAFS spectra of all configurations were averaged for comparison with experiment. The value of ΔE_0 was varied to optimize agreement with experiment, which was the only free parameter in the comparisons to experimental EXAFS spectra. The Fourier transform (FT) was applied to the averaged EXAFS spectra using IFEFFIT[59] in the range $3 \leq k \leq 12$ Å^{-1} (unless stated otherwise), weighted by k^3, and truncated using a Hanning window with dk = 1 Å^{-1}. The simulated time, radius of the cluster used in the FEFF9 calculations, and the size of the supercell were determined from test calculations performed for the case of a single Ba^{2+} cation substituting for Ca^{2+} in calcite (Figure S1 of the SI), which showed that these

parameters were sufficient to obtain converged EXAFS spectra. For each simulation, the disorder parameters, σ^2, were calculated from the mean square relative displacement of the distance r to each of the shells of interest ($\sigma^2 = \langle (r - \langle r \rangle)^2 \rangle$) using the pool of 140 configurations.

RESULTS

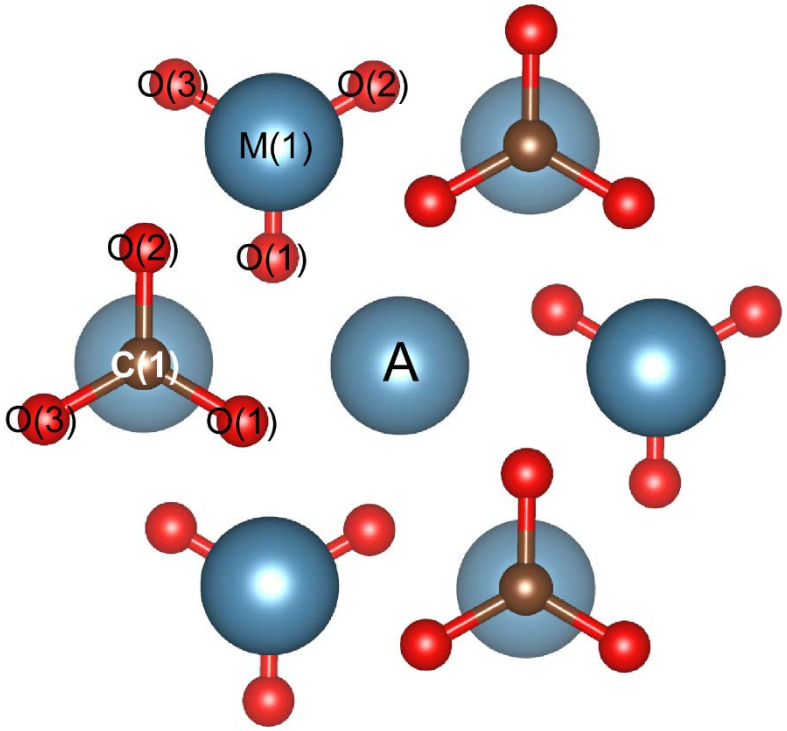

Figure 1. View of the calcite crystal structure (produced by VESTA[60]) down the [001] direction showing all atoms within 4.5 Å of an absorber atom at a calcium site (denoted "A"). The five shells present within this radius are labeled as O(1), C(1), O(2), M(1), and O(3), in order of increasing distance from the absorber.

For each of the seven divalent cations (M^{2+} where M = Ba, Pb, Sr, Cd, Mn, Co, and Zn), the EXAFS spectra calculated at LNT and RT for M^{2+} in MCO_3 and in $CaCO_3$ are presented in this section and compared to experimental spectra when available (Figure 2 to Figure 8). The coordination numbers, distances, and disorder parameters for the first five coordination shells around the absorber atom are presented in Tables S8 to S14 of the SI and are compared to results from shell-by-shell fitting and XRD refinements from the literature. The positions of the first five coordination shells relative to the absorber cation substituting for Ca^{2+} in calcite are illustrated in Figure 1 (see Figure S2 of the SI for an illustration of the coordination shells in aragonite).

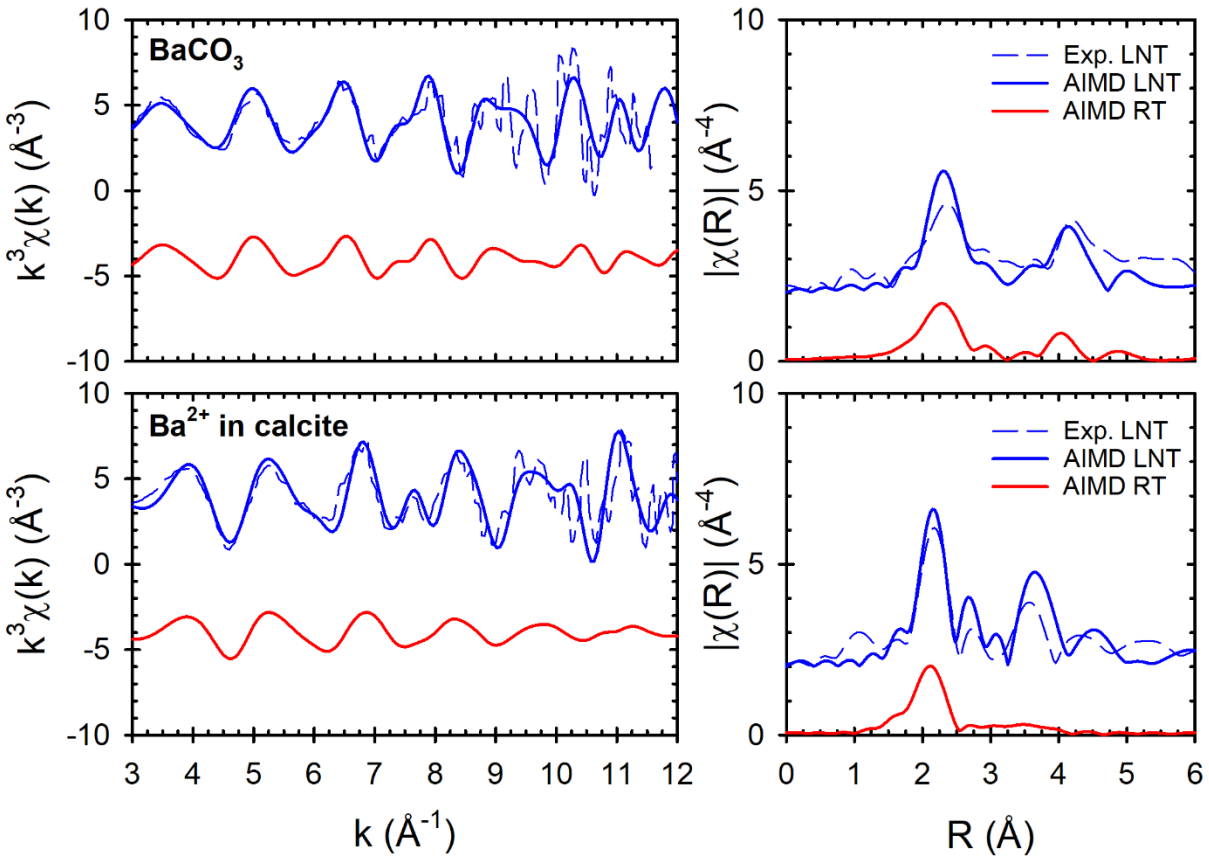

Figure 2. Experimental and calculated Ba K-edge EXAFS spectra (left; ΔE_0 = 0 and −2 eV for $BaCO_3$ and Ba^{2+} in calcite, respectively) and corresponding Fourier transform magnitudes (right; upper *k* range was reduced to 11.5 $Å^{-1}$ for $BaCO_3$ at LNT) for $BaCO_3$ (top) and Ba^{2+} in calcite (bottom) at LNT and RT. The experimental data are from Reeder et al.[2]: "$BaCO_3$ reference" and "Synth. calcite (2125 ppm Ba)" for $BaCO_3$ and Ba^{2+} in calcite, respectively.

$BaCO_3$ and Ba^{2+} incorporation in calcite. The calculated Ba K-edge spectrum of $BaCO_3$ agreed well with the measurements of Reeder et al.[2] at LNT (Figure 2). Given the good agreement between the calculated and experimental amplitudes of the EXAFS signal at low *k*, the differences between the FT magnitudes obtained from the calculated and experimental spectra are attributed to the noise in the experimental data at high *k*. As expected based on the comparison between

calculated and experimental lattice parameters (Table S4), the calculated distances around Ba^{2+} in $BaCO_3$ (Table S8) were in good agreement with those derived from XRD (within ~1%).

The agreement between the calculated spectrum of Ba^{2+} in calcite and that measured at LNT was also good (Figure 2), and, again, the small differences between the FT magnitudes are attributed, for the most part, to the noise in the experimental data. This finding confirmed that Ba^{2+} is in octahedral coordination in calcite with little disorder among the Ba−O bond distances. The peaks beyond the first shell were predicted to essentially disappear in the FT at RT (Figure 2), highlighting the importance of low-temperature measurements for determining the local coordination environment around the impurity. While the shell-by-shell fit reported by Reeder et al.[2] yielded a first coordination shell with parameters in close agreement with the AIMD simulation, the remaining shells had higher coordination numbers and longer distances but much small disorder parameters (Table S8). In particular, the difference between the CNs of the C(1) shell (shell-by-shell fit: 9.6, AIMD: 6.0) was beyond the stated typical uncertainty on CN (20%). The fact that the calculated spectrum was a good match to the experimental data therefore indicates that the original fitting approach did not yield a unique solution, a result of the correlation between CN and σ^2 in an unconstrained fit. This example illustrates how the AIMD-EXAFS approach can provide a more accurate description of the outer coordination shells, especially when they contain weak backscatterers such as C and O.

$PbCO_3$ and Pb^{2+} incorporation in calcite. As for $BaCO_3$, the agreement between calculated and experimental EXAFS spectra of $PbCO_3$ was good, albeit with a small overestimation of the amplitude due to the first coordination shell at LNT (Figure 3). This discrepancy almost disappeared at RT (Figure 3).

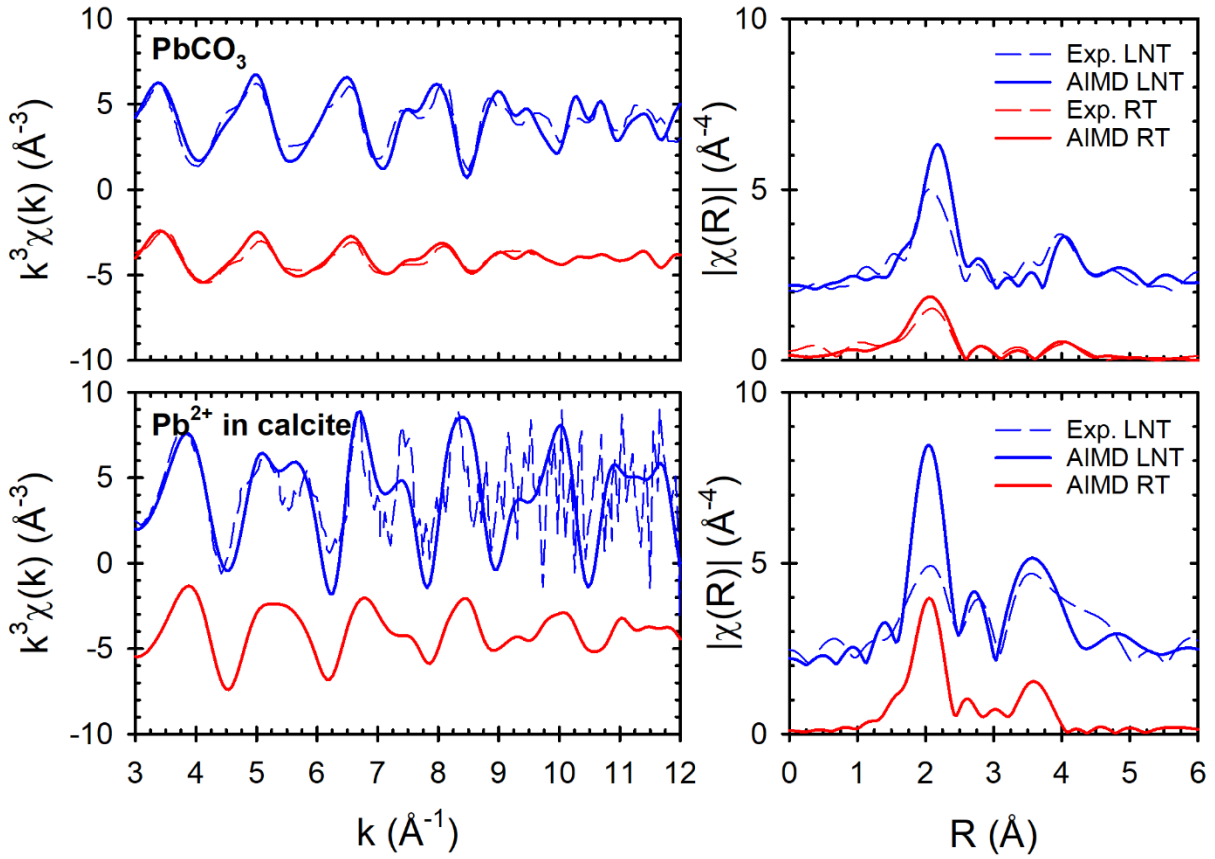

Figure 3. Experimental and calculated Pb L_{III}-edge EXAFS spectra (left; $\Delta E_0 = -5$ and -2 eV for $PbCO_3$ and Pb^{2+} in calcite, respectively) and corresponding Fourier transform magnitudes (right; upper *k* range was reduced to 9.5 $Å^{-1}$ and 10 $Å^{-1}$ for $PbCO_3$ at RT and Pb^{2+} in calcite at LNT, respectively) for $PbCO_3$ (top) and Pb^{2+} in calcite (bottom) at LNT and RT. The experimental data at LNT are from Reeder et al.[2]: "$PbCO_3$ reference" and "Synth. calcite (615 ppm Pb)" for $PbCO_3$ and Pb^{2+} in calcite, respectively; while the experimental data at RT is from Rouff et al.[39]: "cerrusite".

For Pb^{2+} in calcite at LNT, the reciprocal and real space data indicated that the AIMD simulation reproduced well the positions of the coordination shells around Pb^{2+}, but that the intensity of the scattering from the first coordination shell was overestimated in the calculated spectrum (Figure 3). Here the comparison was made difficult by the noise in the data due to the low concentration

of Pb in the synthetic calcite sample. Reeder et al.[2] fitted the experimental spectrum without any constraints and Rouff et al.[39] later refitted the same spectrum with the coordination numbers of the C(1), O(2), and Ca(1) shells fixed to the expected values (Table S9). This experimental spectrum and the fit with constraints were reported again in subsequent publications by the same group.[40-42] The main differences between the AIMD simulation at LNT and the results of the constrained shell-by-shell fit were the longer distance to the O(2) shell in the fit (3.81 Å versus 3.44 Å in the AIMD simulation) and the larger disorder parameter of the first shell (0.005 $Å^2$ versus 0.002 $Å^2$ in the AIMD simulation) (Table S9), which was consistent with the fact that the FT magnitude of the first shell was overestimated by the simulation.

$SrCO_3$ and Sr^{2+} incorporation in calcite. For $SrCO_3$, the calculated Sr K-edge spectra were in good agreement with the experimental data of O'Day et al.[61] at LNT and RT, with only small differences in the amplitudes (Figure 4). Several shell-by-shell fits to $SrCO_3$ EXAFS spectra have been published.[35, 61-65] Only the fits reported by Singer et al.[66] and Pingitore et al.[35] used unconstrained coordination numbers, and these fits resulted in CNs for the first coordination shell (8 and 6.5, respectively) that differed from the known value (9). This example again highlights the potential pitfalls associated with using the shell-by-shell fitting approach to determine CNs with sufficient accuracy to establish, as is often critical, whether the coordination number of an impurity differs from that of the original lattice site it is substituting in.

As pointed out by O'Day et al.[61], resolving second-shell C atoms is difficult due to their weak scattering power, and the fits reported in O'Day et al.[61] therefore only included the three shortest Sr−C(1) distances. The C(1) shell in $SrCO_3$ is split into two subshells resulting in two sets of three Sr−C(1) distances:[67] one at an average distance of 3.03 Å and the other at 3.50 Å. While Parkman et al.[62] constrained CN to be 6 and obtained a value of *R* (3.23 Å) consistent with the average of

the two sets of distances, fits by Finch and Allison[63] and Wallace et al.[65] also fixed CN to 6 but yielded distances that matched that of the inner subshell (3.02 Å and 3.04 Å, respectively). This example illustrates further the difficulties associated with determining the structure of shells occupied by weak backscatterers, even when *R* is less than 4 Å. Contributions from the O(2) and O(3) shells were ignored in the published fits to $SrCO_3$ Sr K-edge spectra (Table S10), as was also done in fits to $PbCO_3$ Pb L_{III}-edge spectra (Table S9). The Sr−M(1) distances obtained in the shell-by-shell fits were generally consistent with those predicted by the AIMD simulations, although the associated disorder parameters varied significantly (Table S10).

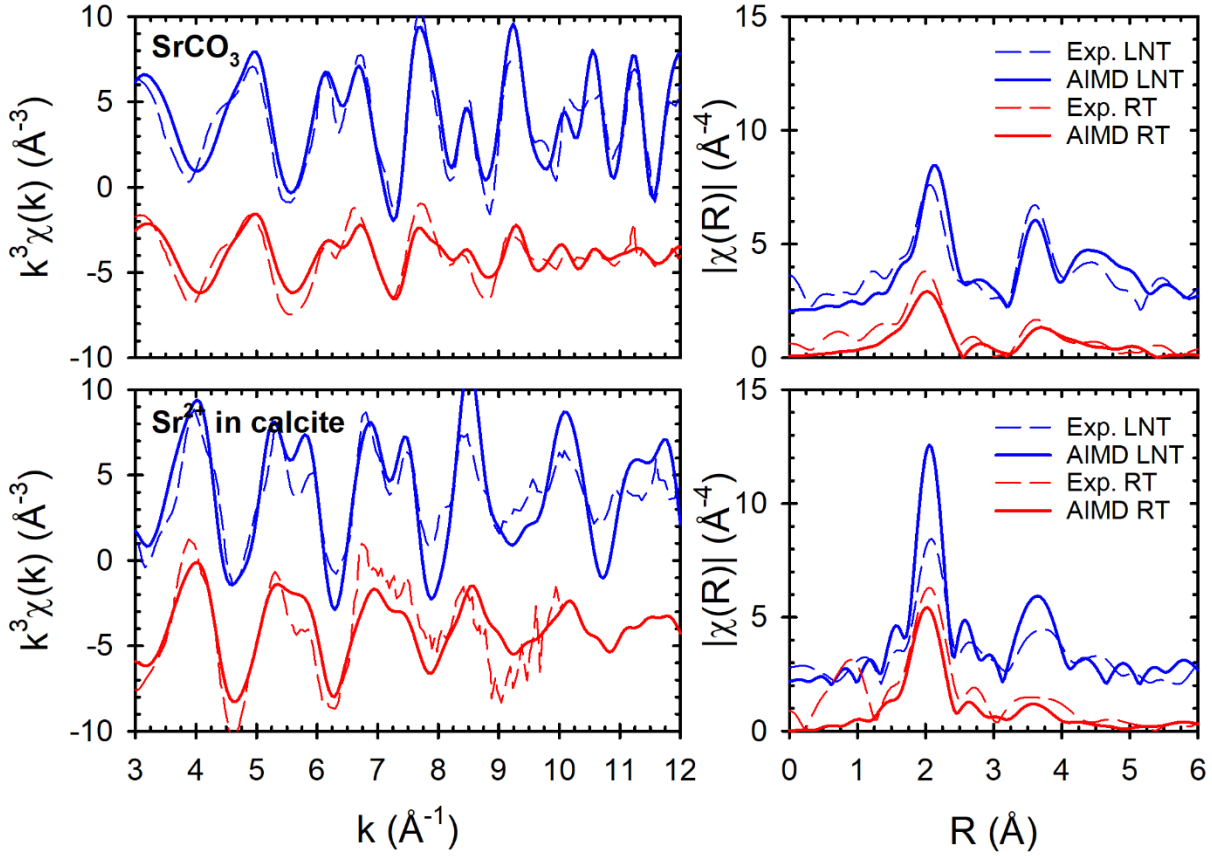

Figure 4. Experimental and calculated Sr K-edge EXAFS spectra (left; ΔE_0 = −8 and 2 eV for $SrCO_3$ and Sr^{2+} in calcite, respectively) and corresponding Fourier transform magnitudes (right; upper *k* range was reduced to 10.8 $Å^{-1}$ for Sr^{2+} in calcite at RT) for $SrCO_3$ (top) and Sr^{2+} in calcite

(bottom) at LNT and RT. The experimental data are from O'Day et al.[61] for $SrCO_3$ and from Littlewood et al.[68] and Pingitore et al.[35] for Sr^{2+} in calcite at LNT and RT, respectively.

For Sr^{2+} in calcite, the calculated Sr K-edge spectra reproduced the main peaks present in the experimental spectra, but it underestimated at LNT the extent of signal attenuation at high *k*, which resulted in overestimated FT magnitudes (Figure 4). This discrepancy was reduced at RT. An early fit by Pingitore et al.,[35] who only considered the first shell, found little compression of the Sr−O bond distance in calcite relative to that in $SrCO_3$, but subsequent fits by other authors[62, 63, 68] showed a more significant compression, in agreement with the AIMD simulations (Table S10).

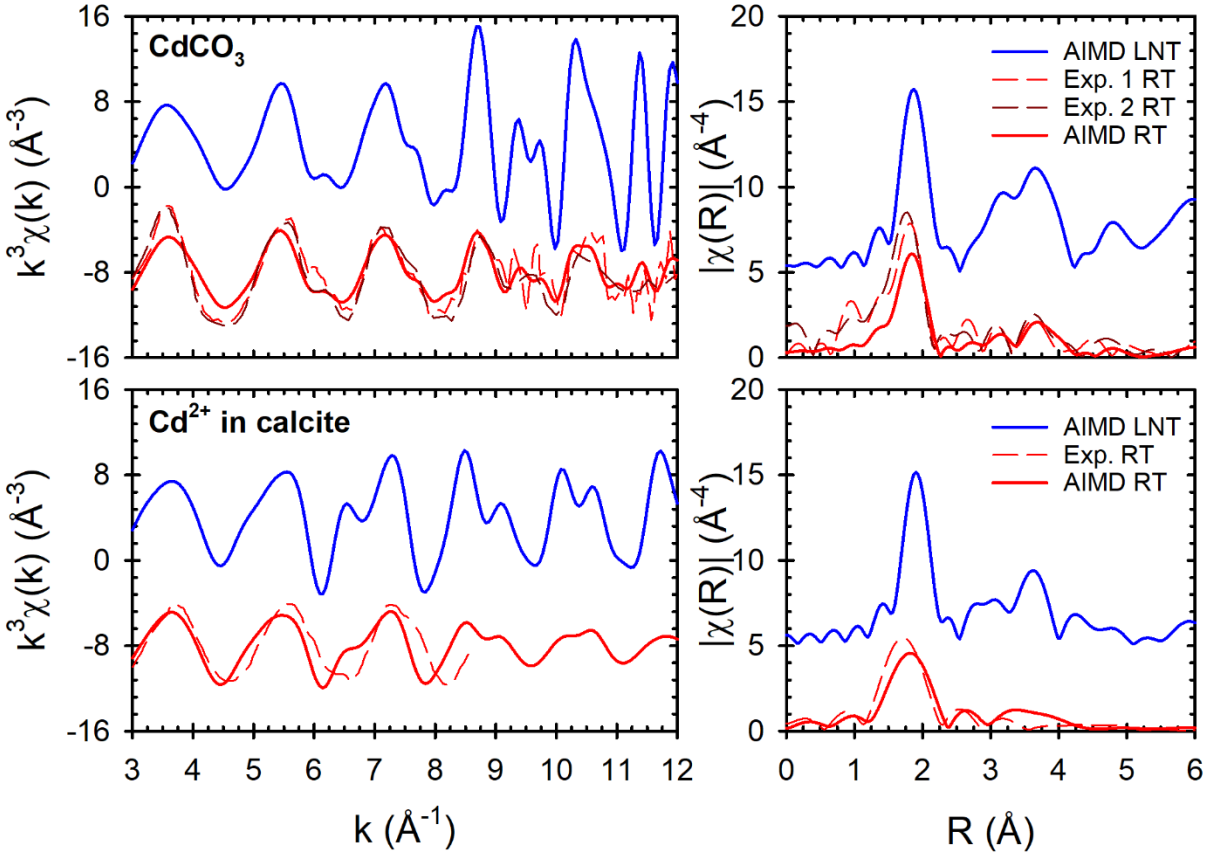

Figure 5. Experimental and calculated Cd K-edge EXAFS spectra (left; ΔE_0 = 2 eV) and corresponding Fourier transform magnitudes (right; upper *k* range was reduced to 8.5 $Å^{-1}$ for Cd^{2+} in calcite at RT) for $CdCO_3$ (top) and Cd^{2+} in calcite (bottom) at LNT and RT. The experimental

data are from Gräfe et al.[69] (Exp. 1) and Sun et al.[70] (Exp. 2) for $CdCO_3$ at RT and from Khaokaew et al.[71] for Cd^{2+} in calcite at RT.

$CdCO_3$ and Cd^{2+} incorporation in calcite. Experimental data for Cd^{2+} in $CdCO_3$ and $CaCO_3$ are relatively scarce and only available at RT. The calculated Cd K-edge spectrum of $CdCO_3$ at RT was in good agreement with the measurements reported by Gräfe et al.[69] and Sun et al.[70] (Figure 5). Sun et al.[70] did not provide the magnitude of $k^3\chi(k)$ and, for the purposes of this comparison, their spectrum was therefore scaled so as to match the intensity of the first peak in the spectrum of Gräfe et al.[69] (at approximately 3.6 $Å^{-1}$). The fits conducted in both studies resulted in high CNs for the first shell (≈7.5) compared to the known value (6). Gräfe et al.[69] noted that this discrepancy may have been due to constructive interference from higher order shells, multiple scattering, and/or disordered states causing larger Debye-Waller parameters. However, the calculated spectrum, which considered the first five shells and all scattering paths with lengths up to 8 Å, suggested that this discrepancy was primarily the result of an increased magnitude of the EXAFS signal at low *k*. Unlike Gräfe et al.,[69] Sun et al.[70] included the O(2) shell in their fit but obtained a long distance (3.92 Å versus 3.40 Å) and a low coordination number (3.4 versus 6) compared to XRD. Their CNs for the C(1) and M(1) shells were also significantly suppressed (1.8 and 4.6, respectively) compared to XRD (6). This comparison illustrates again the effect the large uncertainties on CN may have on shell-by-shell fits as well as the difficulties in resolving weak backscattering atoms beyond the first shell.

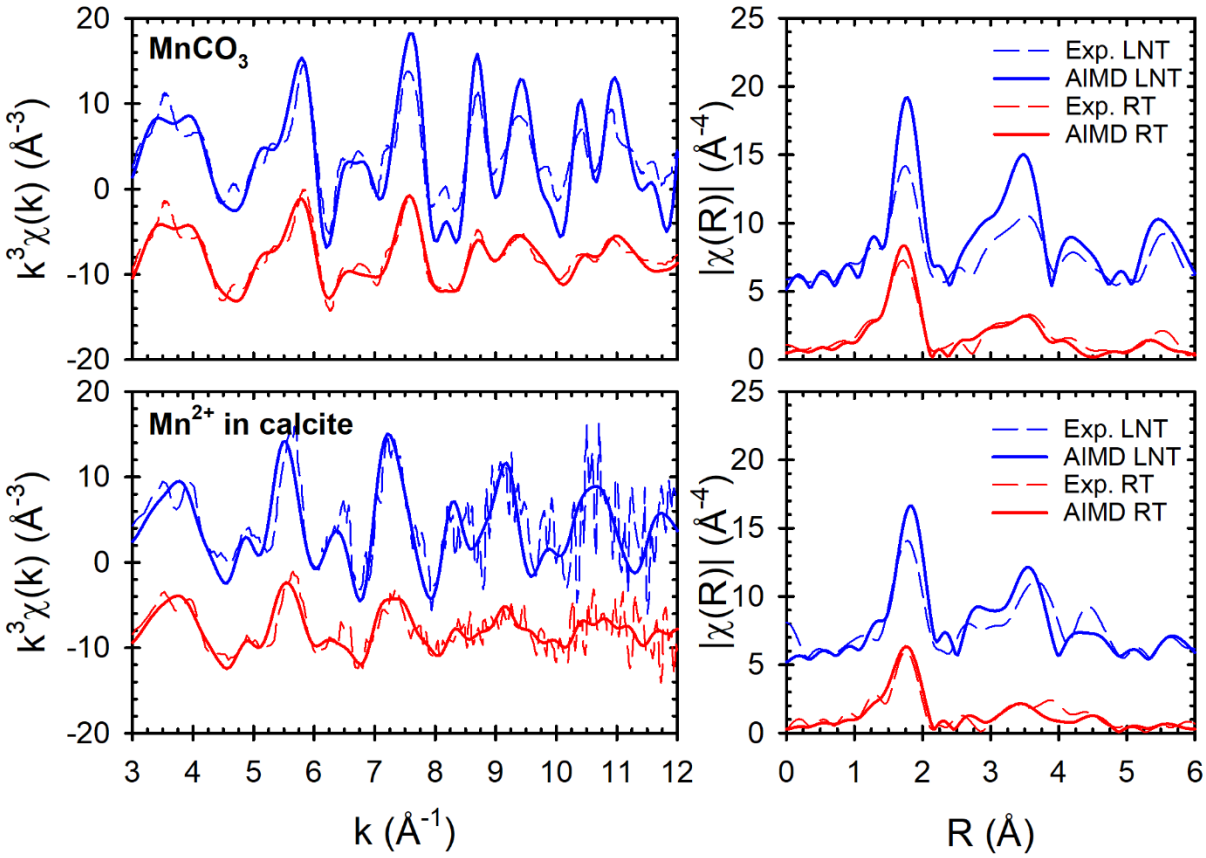

Figure 6. Experimental and calculated Mn K-edge EXAFS spectra (left; $\Delta E_0 = -7$ and -5 eV for $MnCO_3$ and Mn^{2+} in calcite, respectively) and corresponding Fourier transform magnitudes (right) for $MnCO_3$ (top) and Mn^{2+} in calcite (bottom) at LNT and RT. The experimental data are from Lee et al.[37]: synthetic $MnCO_3$ and 0.003 Mn^{2+} in synthetic calcite for $MnCO_3$ and Mn^{2+} in calcite, respectively.

$MnCO_3$ and Mn^{2+} incorporation in calcite. The agreement with the Mn K-edge EXAFS data of Lee et al.[37] was good for Mn^{2+} in both $MnCO_3$ and calcite (Figure 6). One exception was the amplitudes at high k at LNT for Mn^{2+} in $MnCO_3$, which were overestimated in the calculated spectrum. This discrepancy translated to an overestimation by the simulation of the FT magnitudes. As for $PbCO_3$ and $SrCO_3$, this discrepancy disappeared at RT. Lee al.[37] had to use an amplitude factor of 0.75 in their fits to the Mn K-edge spectra whereas a theoretical value of

0.935 was used in this work. An overestimation of the amplitude factor in the calculation could have therefore contributed to the discrepancy. Lee et al.[37] used a comprehensive fitting approach whereby all coordination shells up to 5 Å were included in all the fits. As a result, the distances and disorder parameters were generally in close agreement with those derived from the AIMD simulations (Table S12).

$ZnCO_3$ and Zn^{2+} incorporation in calcite. For $ZnCO_3$, the calculated Zn K-edge spectra reproduced all the peaks present in the measured spectra. However, as *k* increased, the calculated amplitude of the EXAFS signal did not attenuate as appreciably as the experimental signal. Again, this discrepancy was more pronounced at LNT. Consequently, the number and position of the peaks in the calculated FT magnitudes agreed very well with the FT of the experimental spectra, but the magnitudes of the peaks were overestimated.

For Zn^{2+} in calcite, the magnitude of the first-shell peak in the FT of the calculated spectra was overestimated at LNT and underestimated at RT relative to the FT of the corresponding experimental spectra. Because the experimental spectra at the two temperatures were from separate measurements performed and reported by different research groups, these discrepancies may be in part due to experimental uncertainties and issues of reproducibility. The shapes of the peaks corresponding to the C(1) and O(2) shells in the FT of the calculated LNT spectrum differed from those in the FT of the experimental spectrum. This difference may be due to the experimental noise or to the presence of Zn^{2+} in multiple coordination environments, although the good agreement at RT between simulation and experiment for this feature of the Fourier transformed spectrum strongly suggests that Zn^{2+} was only present in the coordination environment considered in the AIMD simulations (i.e. at a calcium site).

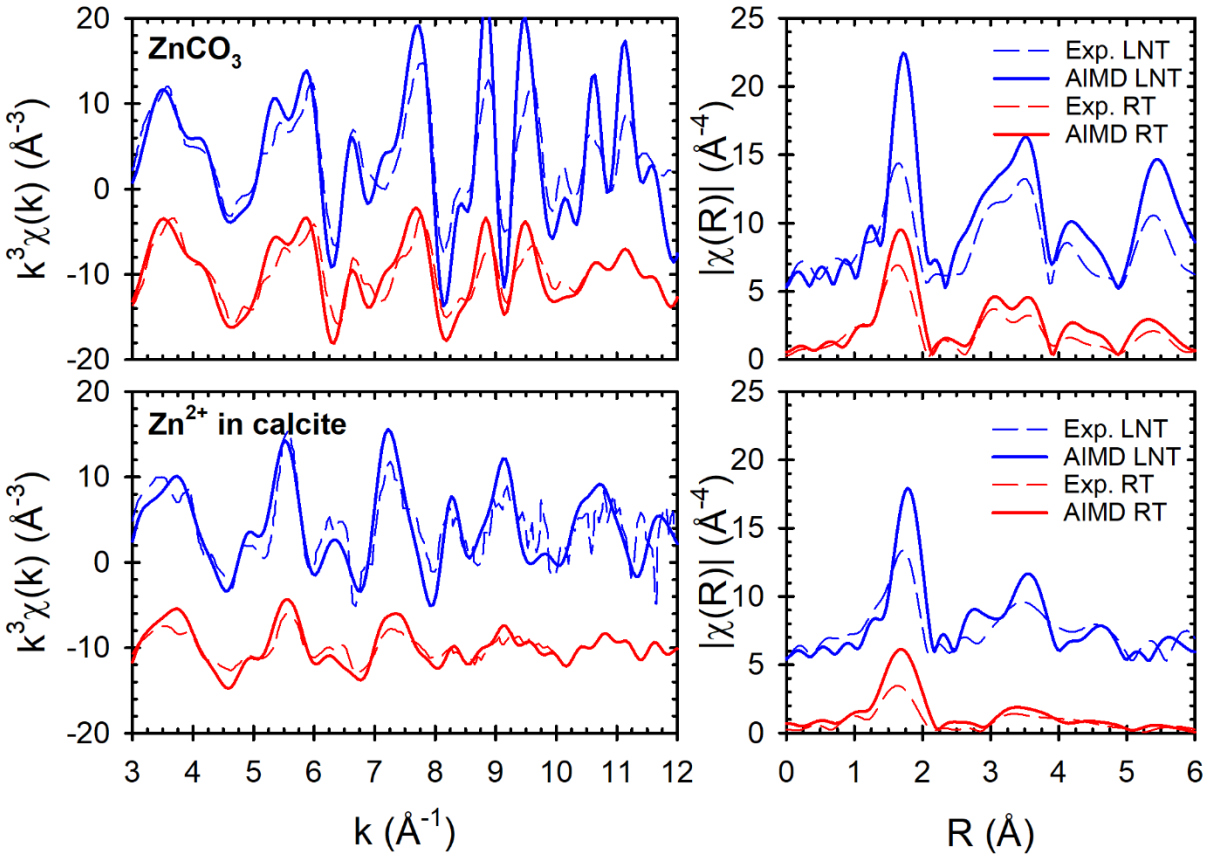

Figure 7. Experimental and calculated Zn K-edge EXAFS spectra (left; $\Delta E_0 = -1$ and 1 eV for $ZnCO_3$ and Zn^{2+} in calcite, respectively) and corresponding Fourier transform magnitudes (right; upper *k* range was reduced to 10.4 $Å^{-1}$ and 9.9 $Å^{-1}$ for $ZnCO_3$ and Zn^{2+} in calcite at RT, respectively) for $ZnCO_3$ (top) and Zn^{2+} in calcite (bottom) at LNT and RT. The experimental data at LNT are from Reeder et al.[2] ("synth. calcite (945 ppm Zn)" for Zn^{2+} in calcite) while the experimental data at RT are from Van Damme et al.[72] and Jacquat et al.[73] for $ZnCO_3$ and Zn^{2+} in calcite, respectively.

$CoCO_3$ and Co^{2+} incorporation in calcite. As for the Zn K-edge spectra of $ZnCO_3$, the calculated Co K-edge spectra of $CoCO_3$ overestimated the amplitudes of the EXAFS signals, particularly at high *k* and at low temperature. The spectrum measured at RT only had data up to 7.9 $Å^{-1}$, and the FT was therefore applied to this reduced *k* range, in addition to the default *k* range

($3 \leq k \leq 12$ Å^{-1}). The difference between the two FT spectra of the same EXAFS spectrum highlights the importance of using consistent FT parameters when comparing spectra.

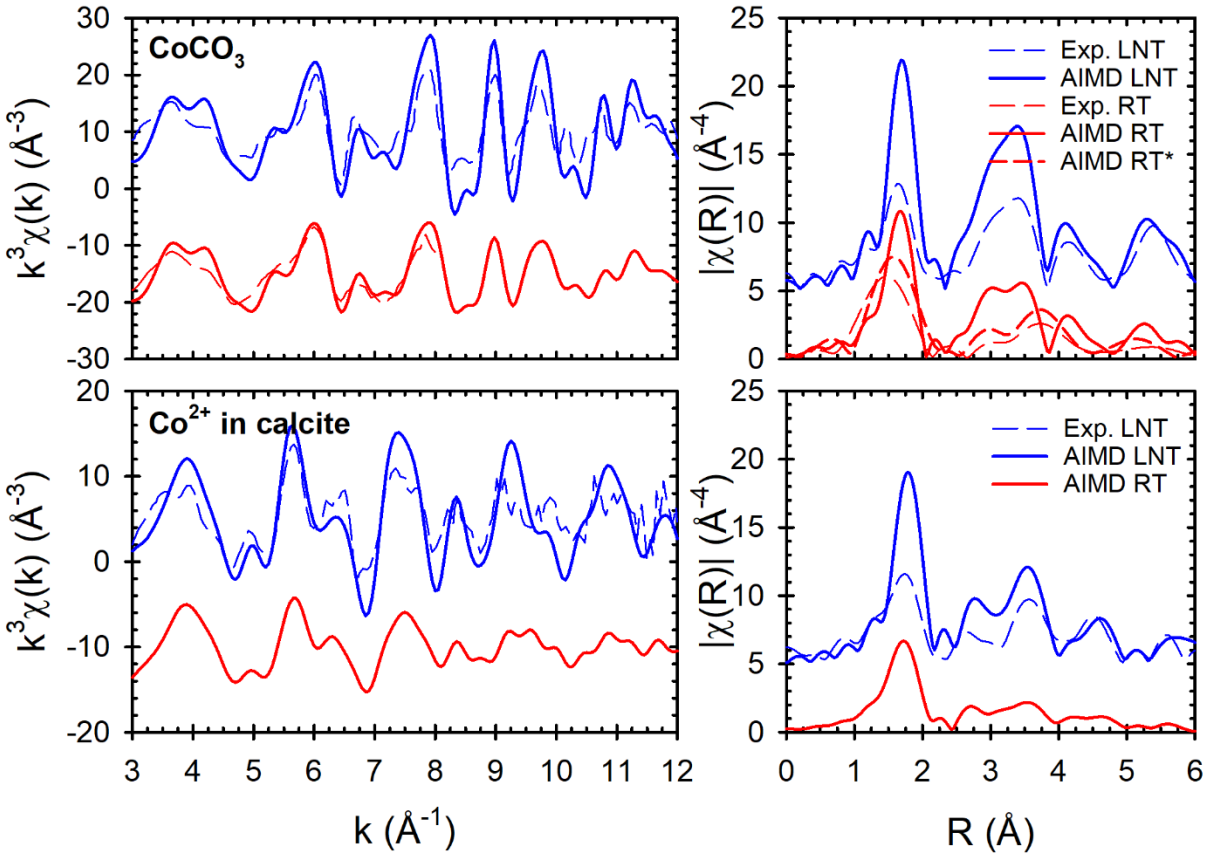

Figure 8. Experimental and calculated Co K-edge EXAFS spectra (left; $\Delta E_0 = -5$ and 0 eV for $CoCO_3$ and Co^{2+} in calcite, respectively) and corresponding Fourier transform magnitudes (right; upper k range was reduced to 7.9 Å^{-1} for $CoCO_3$ at RT for the spectrum marked with a '*') for $CoCO_3$ (top) and Co^{2+} in calcite (bottom) at LNT and RT. The experimental data at LNT are from Reeder et al.[2] ("$CoCO_3$ reference" and "synth. calcite (2150 ppm Co)" for $CoCO_3$ and Co^{2+} in calcite, respectively) while the experimental data at RT are from Cheng et al.[74] for $CoCO_3$.

For Co^{2+} in calcite at LNT, the calculated spectrum reproduced well the peaks present in the measured EXAFS spectrum, but the amplitudes were again overestimated. This observation was consistent with the fact that the fit to this EXAFS spectrum reported by Reeder et al.[2] yielded

distances in agreement with the AIMD simulation, but disorder parameters that were larger than those derived from the simulation (Table S14). Several factors could contribute to this discrepancy including an overestimation of the amplitude factor, a significant partitioning of Co^{2+} at the sample's surface, and experimental uncertainties.

DISCUSSION

Overall, the theoretical predictions of the EXAFS spectra over the range of systems considered was good, exhibiting a one-to-one correspondence between features in the predicted and measured spectra. The AIMD-based predictions were ab initio in the sense that the only parameter adjusted to improve agreement with the measurements was ΔE_0. In particular, the effect of thermal motion was treated with no adjustable parameters. Still, the positions and amplitudes of the measured spectra were well reproduced in most cases. Careful examination of the spectra showed that the remaining disagreement consisted largely of too high amplitudes of the EXAFS signal at high k in the theoretical predictions relative to the measurements. This behavior is consistent with the presence in the measured samples of static, structural disorder, which is absent in the periodic computer simulations. To test the ability of structural disorder to explain the residual disagreement, the K-edge spectrum of Zn^{2+} in $ZnCO_3$ at LNT (top left panel of Figure 7) was plotted against the theoretical predictions including an additional multiplicative factor (i.e., affecting every scattering path equally) $\exp(-\sigma_s^2 k^2)$ where σ_s^2 is a disorder parameter attributed to nonthermal disorder[12] (e.g., departures from perfect crystallinity, particle surfaces, grain boundaries, etc.). This comparison (with the physically reasonable σ_s^2 = 0.0076 Å) is presented in Figure 9. This comparison indicates that the AIMD simulations faithfully reproduced the EXAFS up to effects from imperfect crystallinity of the samples. Aside from Figure 9, all the AIMD-EXAFS results include no additional damping for static disorder.

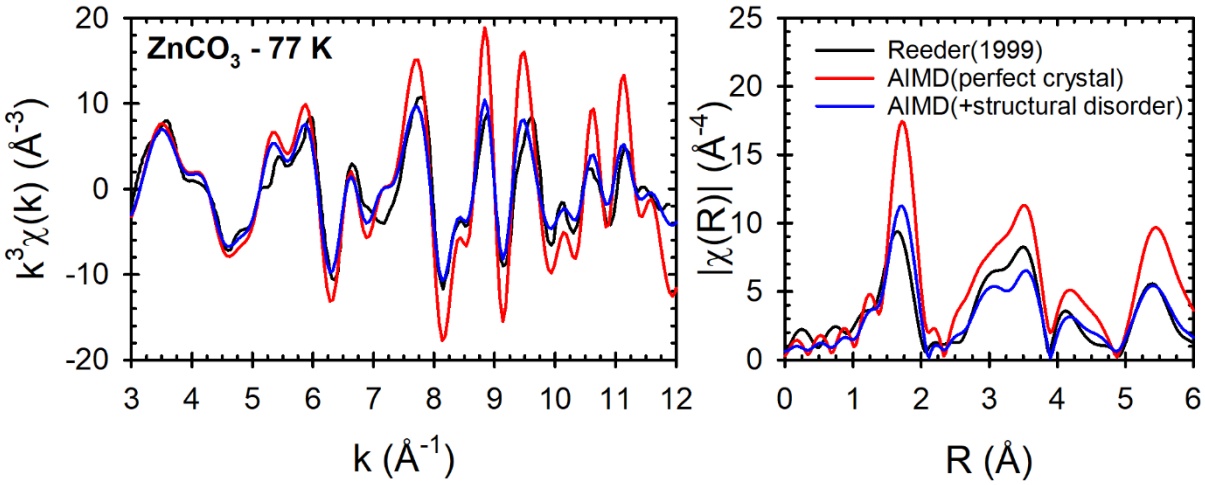

Figure 9. Experimental and calculated Zn K-edge EXAFS spectra (left; $\Delta E_0 = -1$ eV) and corresponding Fourier transform magnitudes (right) of $ZnCO_3$ at LNT, with and without structural disorder accounted for by a disorder parameter ($\sigma_s^2 = 0.0076$ Å^2). The experimental spectrum is from Reeder et al.[2].

The agreement between the predicted and measured EXAFS spectra implied that the AIMD simulations captured well the coordination environment around the impurities in calcite. In particular, the simulations confirmed that all the divalent cations considered in this work are incorporated in calcite via substitution at the calcium site. Therefore, information from individual simulations can be combined to develop a comprehensive view of the structural changes associated with introducing divalent cation impurities of varying sizes. Calculated distances from the impurity to atoms in the first five coordination shells in MCO_3 and $CaCO_3$ at both temperatures are compared in Figure 10 to those derived from shell-by-shell fits to EXAFS data and from XRD refinements, where available.

For M^{2+} in MCO_3, the calculated distances were in general good agreement with those derived from shell-by-shell fitting, and the two methods also generally agree with XRD refinements. There were however several outliers that highlight potential issues with the shell-by-shell fitting

approach even for this simple case where the structures are known. As discussed above, several fits either only included the inner C(1) subshell in $PbCO_3$ and $SrCO_3$, leading to an incomplete coordination environment, or included the complete shell but at a distance corresponding to the inner subshell. Additionally, O(2) and O(3) shells were rarely included in the fits, and, when they were, the resulting distances were often not accurate (e.g. slight discrepancies for Mn^{2+}−O(2) and Mn^{2+}−O(3) and significant discrepancy for Cd^{2+}−O(2)). These observations underline the difficulties in resolving weak backscatterers in coordination shells beyond the first shell even when constraints can be applied on the basis of the known structure.

For M^{2+} in $CaCO_3$, the agreement between AIMD simulations and shell-by-shell fitting was good for the first (M−O(1), light backscatterers but short distances) and fourth (M−Ca(1), long distances but heavy backscatterers) shells. The largest discrepancies were found for the second and third shells (M−O(2) and M−C(1), combination of light backscatterers and long distances) shells and the fifth shell (M−O(3)) was usually absent. Additionally, AIMD simulations showed only small differences between RT and LNT distances while shell-by-shell fitting led to significant differences in several instances. The most significant difference between the two methods was the trend followed by the M−O(2) distances for cations larger than Ca^{2+}. Shell-by-shell fitting indicated a positive correlation to Δr whereas the simulations showed the opposite trend. In other words, as the calcite structure expands upon substitution by the larger cations, nearest-neighbor carbonate groups rotate to decrease the distance between one set of distant carbonate oxygen atoms, a detail missed in the shell-by-shell fits.

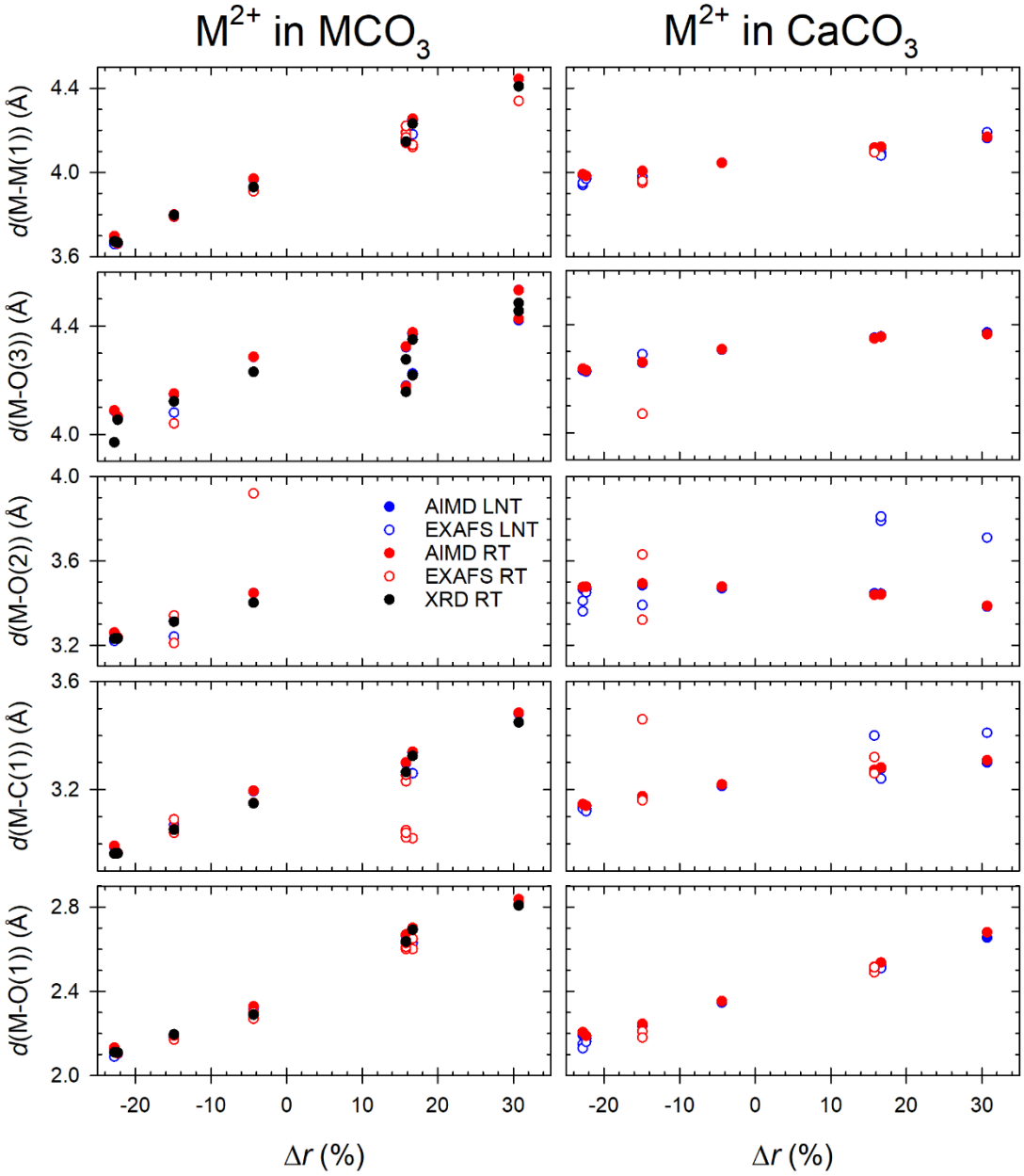

Figure 10. Calculated inter-atomic distances between the absorber (M) and backscattering atoms in the first five coordination shells as a function of the percentage change in ionic radius with respect to Ca^{2+}. The Δr values are 30.7, 16.7, 15.8, −4.4, −14.9, −22.4, and −22.8 for Ba^{2+}, Pb^{2+}, Sr^{2+}, Cd^{2+}, Mn^{2+}, Co^{2+}, and Zn^{2+}, respectively. Data are presented for M^{2+} in MCO_3 (left) and $CaCO_3$ (right). Also shown are the distances obtained from shell-by-shell fitting at LNT and RT and from refinements of XRD data at RT.

The calculated disorder parameters of the first five coordination shells around the impurities are summarized and compared to those determined from shell-by-shell fitting in Figure 11. Using Ba^{2+} (Δr = 30.7%), Cd^{2+} (Δr = −4.4%), and Co^{2+} (Δr = −22.4%) in calcite as examples, Figure S3 shows that the distributions of distances from the absorber to the first five coordination shells are well represented by a symmetric Gaussian distribution, thus supporting the use of symmetric thermal disorder parameters. For M^{2+} in MCO_3, the data showed more variations between shell-by-shell fits of the same system than observed for the inter-atomic distances. Additionally, the calculated and fitted disorder parameters also more frequently differed than for the inter-atomic distances. These differences between R and σ^2 are attributed to the potential correlation between CN and σ^2 and the fact that σ^2 is more sensitive to noise in the measurements. For the first coordination shell, both approaches displayed a step increase when going from negative to positive Δr and an increase when going from LNT to RT. For the cations larger than Ca^{2+}, shell-by-shell fits overestimated σ^2 at LNT but underestimated it at RT, leading to a reduced difference between the values at the two temperatures relative to the AIMD simulations.

As previously discussed, M−C(1) is split into two subshells for carbonates with the aragonite structure. This split translated to relatively large σ^2 calculated form the AIMD simulations for the shell as a whole compared to the values obtained for carbonates with the calcite structure. If only the inner subshell was considered, as was done in several fits, σ^2 decreased, however several fits used the shorter R and lower σ^2 to represent the entire shell. The data for the O(2) and O(3) shells were limited as these shells were often not included in the fits. As for the first shell, the disorder parameters of the M(1) shell showed large variations, especially for the cations larger than Ca^{2+}.

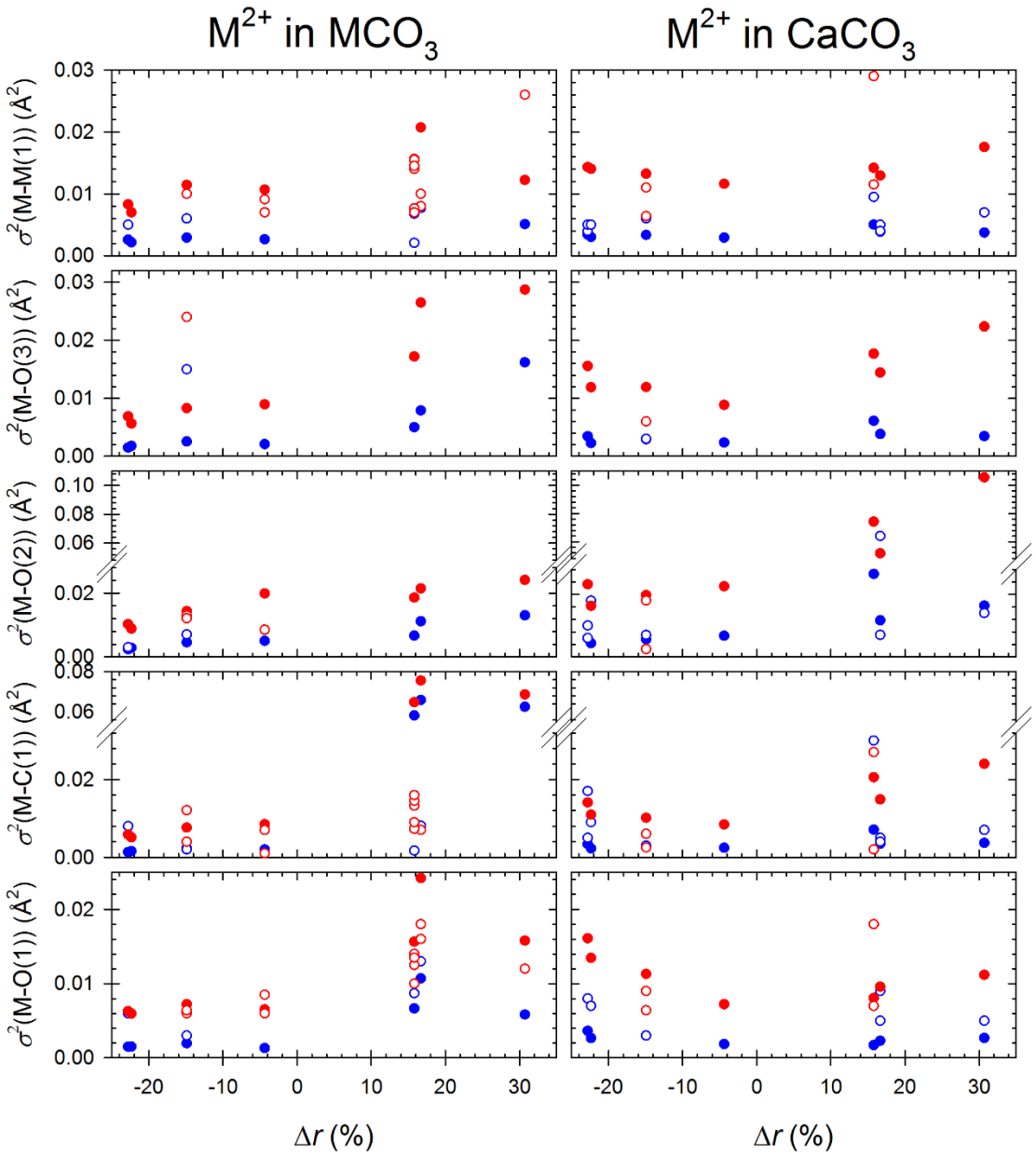

Figure 11. Calculated disorder parameters (solid circles) of the first five coordination shells around the absorber (M) as a function of the percentage change in ionic radius with respect to Ca^{2+} at LNT (blue circles) and RT (red circles). The Δr values are 30.7, 16.7, 15.8, −4.4, −14.9, −22.4, and −22.8 for Ba^{2+}, Pb^{2+}, Sr^{2+}, Cd^{2+}, Mn^{2+}, Co^{2+}, and Zn^{2+}, respectively. Data are presented for M^{2+} in MCO_3 (left) and $CaCO_3$ (right). Also shown are the disorder parameters obtained from shell-by-shell fitting (empty circles) at LNT (blue circles) and RT (red circles).

As for M^{2+} in MCO_3, the agreement between the disorder parameters obtained from the two methods for the impurities incorporated in calcite was worse than for the distances, even for the more easily resolved shells, i.e. O(1) and M(1). Moreover, the AIMD simulations predicted that all shells except O(2) display a U-shaped dependence of σ^2 on Δr. In other words, the disorder parameter increased as the magnitude of the change in ionic radius with respect to Ca^{2+} increased. This trend was not well defined by the shell-by-shell fits due to the more limited dataset and the more extensive variations than in the AIMD simulations.

CONCLUSIONS

AIMD simulations of seven divalent metal cations incorporated in calcite and of their corresponding endmember carbonate phases were performed at 77 K and 298.15 K. The atomic trajectories were then used to calculate EXAFS spectra, which were compared to experimental spectra published in the literature, where available. Comparison of the calculated and experimental spectra confirmed that all seven divalent cation impurities incorporated in calcite via substitution in the calcium site.

The most significant discrepancies between the AIMD simulations and the results of shell-by-shell fits to the experimental spectra included the coordination numbers, inter-atomic distances, and disorder parameters of the C(1), O(2), and O(3) shells. This finding highlights the difficulties in resolving weak backscatterers beyond the first coordination shell in shell-by-shell fits, a limitation that the AIMD-EXAFS approach can overcome. As a result, previously-missed details of the nature and extent of the structural relaxation around the impurities emerged from the simulations. For example, as the calcite structure expands around the impurities for divalent cations larger than Ca^{2+}, nearest-neighbor carbonates also rotate resulting in a compression of the M−O(2) distances. The simulations also clearly showed that, except for the O(2) shells, the

disorder parameters of all the shells increased as the magnitude of the change in ionic radius upon substitution increased.

The approach used in this work is therefore a powerful approach to interpret EXAFS data and extract accurate structural information. This improved accuracy is expected to enable a determination of charge compensation schemes associated with the incorporation of aliovalent impurities in calcite, such as rare-earth cations.[3]

ACKNOWLEDGMENTS

This work was supported by the U.S. Department of Energy (DOE), Office of Science, Office of Basic Energy Sciences, Chemical Sciences, Geosciences, and Biosciences Division through its Geosciences Program at Pacific Northwest National Laboratory (PNNL). PNNL is operated for DOE by Battelle Memorial Institute under Contract DE-AC05-76RL01830. All the simulations were performed using the Environmental Molecular Sciences Laboratory (EMSL), a national scientific user facility sponsored by the U.S. DOE's Office of Biological and Environmental Research and located at PNNL in Richland, WA.

AUTHOR INFORMATION

Corresponding Author

*Phone: (509) 371-6382; e-mail: sebastien.kerisit@pnnl.gov.

SUPPORTING INFORMATION

Calcite and aragonite lattice parameters and total energy per stoichiometric unit as a function of the number of *k*-points and of the plane-wave energy cutoff; comparison of experimental and calculated (PBE, PBE/D3, RPBE, RPBE/D3, PBE0) lattice parameters for a range of carbonates with either the aragonite or the calcite structure; calculated Ba K-edge EXAFS spectra of Ba^{2+} in calcite as a function of cluster radius, simulated time, and calcite supercell size; coordination environment of M^{2+} in MCO_3 (M = Ba, Pb, Sr, Cd, Mn, Co, or Zn) and $CaCO_3$ obtained from AIMD simulations at liquid nitrogen and room temperature, and, where available, comparison with results of shell-by-shell fits to EXAFS spectra and XRD refinements published in the literature; atomic model of aragonite structure around calcium site; distributions of inter-atomic distances between Ba^{2+}, Cd^{2+}, or Co^{2+} impurity and atoms in their first five coordination shells from AIMD simulations at liquid nitrogen temperature.

REFERENCES

1. Stumm, W.; Morgan, J. J., *Aquatic Chemistry*. Wiley-Interscience: New York, USA, 1996.

2. Reeder, R. J.; Lamble, G. M.; Northrup, P. A., XAFS study of the coordination and local relaxation around Co^{2+}, Zn^{2+}, Pb^{2+}, and Ba^{2+} trace elements in calcite. *Am. Miner.* **1999,** *84*, 1049-1060.

3. Elzinga, E. J.; Reeder, R. J.; Withers, S. H.; Peale, R. E.; Mason, R. A.; Beck, K. M.; Hess, W. P., EXAFS study of rare-earth element coordination in calcite. *Geochim. Cosmochim. Acta* **2002,** *66*, 2875-2885.

4. Hellebrandt, S. E.; Hofmann, S.; Jordan, N.; Barkleit, A.; Schmidt, M., Incorporation of Eu(III) into calcite under recrystallization conditions. *Sci. Rep.* **2016,** *6*, 33137.

5. Sturchio, N. C.; Antonio, M. R.; Soderholm, L.; Sutton, S. R.; Brannon, J. C., Tetravalent uranium in calcite. *Science* **1998,** *281*, 971-973.

6. Reeder, R. J.; Nugent, M.; Lamble, G. M.; Tait, C. D.; Morris, D. E., Uranyl incorporation into calcite and aragonite: XAFS and luminescence studies. *Environ. Sci. Technol.* **2000,** *34*, 638-644.

7. Kelly, S. D.; Newville, M. G.; Cheng, L.; Kemner, K. M.; Sutton, S. R.; Fenter, P.; Sturchio, N. C.; Spötl, C., Uranyl incorporation in natural calcite. *Environ. Sci. Technol.* **2003,** *37*, 1284-1287.

8. Balboni, E.; Morrison, J. M.; Wang, Z.; Engelhard, M. H.; Burns, P. C., Incorporation of Np(V) and U(VI) in carbonate and sulfate minerals crystallized from aqueous solution. *Geochim. Cosmochim. Acta* **2015,** *151*, 133-149.

9. Tang, Y.; Elzinga, E. J.; Lee, Y. J.; Reeder, R. J., Coprecipitation of chromate with calcite: Batch experiments and X-ray absorption spectroscopy. *Geochim. Cosmochim. Acta* **2007,** *71*, 1480-1493.

10. Alexandratos, V. G.; Elzinga, E. J.; Reeder, R. J., Arsenate uptake by calcite: Macroscopic and spectroscopic characterization of adsorption and incorporation mechanisms. *Geochim. Cosmochim. Acta* **2007,** *71*, 4172-4187.

11. Podder, J.; Lin, J.; Sun, W.; Botis, S. M.; Tse, J.; Chen, N.; Hu, Y.; Li, D.; Seaman, J.; Pan, Y., Iodate in calcite and vaterite: Insights from synchrotron X-ray absorption spectroscopy and first-principles calculations. *Geochim. Cosmochim. Acta* **2017,** *198*, 218-228.

12. Rehr, J. J.; Albers, R. C., Theoretical approaches to x-ray absorption fine structure. *Rev. Mod. Phys.* **2000,** *72*, 621.

13. D'Angelo, P.; Di Nola, A.; Filipponi, A.; Pavel, N. V.; Roccatano, D., An extended X-ray absorption fine structure study of aqueous solutions by employing molecular dynamics simulations. *J. Chem. Phys.* **1994,** *100*, 985-994.

14. Palmer, B. J.; Pfund, D. M.; Fulton, J. L., Direct modeling of EXAFS spectra from molecular dynamics simulations. *J. Phys. Chem.* **1996,** *100*, 13393-13398.

15. Campbell, L.; Rehr, J. J.; Schenter, G. K.; McCarthy, M. I.; Dixon, D., XAFS Debye-Waller factors in aqueous Cr+3 from molecular dynamics. *J. Synchrotron Rad.* **1999,** *6*, 310-312.

16. Merkling, P. J.; Muñoz-Páez, A.; Martínez, J. M.; Pappalardo, R. R.; Sánchez Marcos, E., Molecular-dynamics-based investigation of scattering path contributions to the EXAFS spectrum: The Cr^{3+} aqueous solution case. *Physical Review B* **2001,** *64*, 012201.

17. Cauët, E.; Bogatko, S.; Weare, J. H.; Fulton, J. L.; Schenter, G. K.; Bylaska, E. J., Structure and dynamics of the hydration shells of the Zn^{2+} ion from ab initio molecular dynamics and combined ab initio and classical molecular dynamics simulations. *J. Chem. Phys.* **2010,** *132*, 194502.

18. Atta-Fynn, R.; Bylaska, E. J.; Schenter, G. K.; de Jong, W. A., Hydration shell structure and dynamics of curium(III) in aqueous solution: First principles and empirical studies. *J. Phys. Chem. A* **2011,** *115*, 4665-4677.

19. Fulton, J. L.; Bylaska, E. J.; Bogatko, S.; Balasubramanian, M.; Cauët, E.; Schenter, G. K.; Weare, J. H., Near-quantitative agreement of model-free DFT-mD predictions with XAFS observations of the hydration structure of highly charged transition-metal ions. *J. Phys. Chem. Lett.* **2012,** *3*, 2588-2593.

20. Bogatko, S.; Cauët, E.; Bylaska, E. J.; Schenter, G. K.; Fulton, J. L.; Weare, J. H., The aqueous Ca^{2+} system, in comparison with Zn^{2+}, Fe^{3+}, and Al^{3+}: An ab initio molecular dynamics study. *Chem. Euro. J.* **2013,** *19*, 3047-3060.

21. Kerisit, S.; Bylaska, E. J.; Massey, M. S.; McBriarty, M. E.; Ilton, E. S., Ab initio molecular dynamics of uranium incorporated in goethite (α-FeOOH): Interpretation of X-ray absorption spectroscopy of trace polyvalent metals. *Inorg. Chem.* **2016,** *55*, 11736-11746.

22. McBriarty, M. E.; Soltis, J. A.; Kerisit, S.; Qafoku, O.; Bowden, M. E.; Bylaska, E. J.; De Yoreo, J. J.; Ilton, E. S., Trace uranium partitioning in a multiphase nano-FeOOH system. *Environ. Sci. Technol.* **2017,** *51*, 4970-4977.

23. McBriarty, M. E.; Kerisit, S.; Bylaska, E. J.; Shaw, S.; Morris, K.; Ilton, E. S., Iron vacancies accommodate uranyl incorporation into hematite. *Environ. Sci. Technol.* **2018,** *52*, 6282-6290.

24. Demichelis, R.; Raiteri, P.; Gale, J. D.; Dovesi, R., A new structural model for disorder in vaterite from first-principles calculations. *Cryst. Eng. Comm.* **2012,** *14*, 44-47.

25. Demichelis, R.; Raiteri, P.; Gale, J. D.; Dovesi, R., The multiple structures of vaterite. *Crystal Growth & Design* **2013,** *13*, 2247-2251.

26. Aurelio, G.; Fernández-Martínez, A.; Cuello, G. J.; Román-Ross, G.; Alliot, I.; Charlet, L., Structural study of selenium(IV) substitutions in calcite. *Chem. Geol.* **2010,** *270*, 249-256.

27. Heberling, F.; Vinograd, V. L.; Polly, R.; Gale, J. D.; Heck, S.; Rothe, J.; Bosbach, D.; Geckeis, H.; Winkler, B., A thermodynamic adsorption/entrapment model for selenium(IV) coprecipitation with calcite. *Geochim. Cosmochim. Acta* **2014,** *134*, 16-38.

28. Shuller-Nickles, L. C.; Bender, W. M.; Walker, S. M.; Becker, U., Quantum-mechanical methods for quantifying incorporation of contaminants in proximal minerals. *Minerals* **2014,** *4*, 690-715.

29. Arroyo-de Dompablo, M. E.; Fernández-González, M. A.; Fernández-Díaz, L., Computational investigation of the influence of tetrahedral oxoanions (sulphate, selenate and chromate) on the stability of calcium carbonate polymorphs. *RSC Adv.* **2015,** *5*, 59845-59852.

30. Walker, S. M.; Becker, U., Uranyl(VI) and neptunyl(V) incorporation in carbonate and sulfate minerals: Insight from first-principles. *Geochim. Cosmochim. Acta* **2015,** *161*, 19-35.

31. Balan, E.; Pietrucci, F.; Gervais, C.; Blanchard, M.; Schott, J.; Gaillardet, J., First-principles study of boron speciation in calcite and aragonite. *Geochim. Cosmochim. Acta* **2016,** *193*, 119-131.

32. Polly, R.; Heberling, F.; Schimmelpfennig, B.; Geckeis, H., Quantum chemical investigation of the selenite incorporation into the calcite (10-14) surface. *J. Phys. Chem. C* **2017,** *121*, 20217-20228.

33. Kerisit, S. N.; Smith, F. N.; Saslow, S. A.; Hoover, M. E.; Lawter, A. R.; Qafoku, N. P., Incorporation modes of iodate in calcite. *Environ. Sci. Technol.* **2018,** *52*, 5902-5910.

34. Saslow, S. A.; Kerisit, S. N.; Varga, T.; Johnson, K. C.; Avalos, N. M.; Lawter, A. R.; Qafoku, N. P., Chromate effect on iodate incorporation into calcite. *ACS Earth Space Chem.* **2019,** *3*, 1624-1630.

35. Pingitore, N. E.; Lytle, F. W.; Davies, B. M.; Eastman, M. P.; Eller, P. G.; Larson, E. M., Mode of incorporation of Sr^{2+} in calcite: Determination by X-ray absorption spectroscopy. *Geochim. Cosmochim. Acta* **1992,** *56,* 1531-1538.

36. Lamble, G. M.; Reeder, R. J.; Northrup, P. A., Characterization of heavy metal incorporation in calcite by XAFS spectroscopy. *Journal de Physique IV (France)* **1997,** *7,* 793-797.

37. Lee, Y. J.; Reeder, R. J.; Wenskus, R. W.; Elzinga, E. J., Structural relaxation in the $MnCO_3$-$CaCO_3$ solid solution: A Mn K-edge EXAFS study. *Phys. Chem. Minerals* **2002,** *29,* 585-594.

38. Elzinga, E. J.; Reeder, R. J., X-ray absorption spectroscopy study of Cu^{2+} and Zn^{2+} adsorption complexes at the calcite surface: Implications for site-specific metal incorporation preferences during calcite crystal growth. *Geochim. Cosmochim. Acta* **2002,** *66,* 3943-3954.

39. Rouff, A. A.; Elzinga, E. J.; Reeder, R. J.; Fisher, N. S., X-ray absorption spectroscopic evidence for the formation of Pb(II) inner-sphere adsorption complexes and precipitates at the calcite-water interface. *Environ. Sci. Technol.* **2004,** *38,* 1700-1707.

40. Rouff, A. A.; Elzinga, E. J.; Reeder, R. J.; Fisher, N. S., The influence of pH on the kinetics, reversibility and mechanisms of Pb(II) sorption at the calcite-water interface. *Geochim. Cosmochim. Acta* **2005,** *69,* 5173-5186.

41. Elzinga, E. J.; Rouff, A. A.; Reeder, R. J., The long-term fate of Cu^{2+}, Zn^{2+}, and Pb^{2+} adsorption complexes at the calcite surface: An X-ray absorption spectroscopy study. *Geochim. Cosmochim. Acta* **2006,** *70,* 2715-2725.

42. Rouff, A. A.; Elzinga, E. J.; Reeder, R. J.; Fisher, N. S., The effect of aging and pH on Pb(II) sorption processes at the calcite-water interface. *Environ. Sci. Technol.* **2006,** *40*, 1792-1798.

43. Kresse, G.; Furthmuller, J., Efficient iterative schemes for ab initio total-energy calculations using a plane-wave basis set. *Physical Review B* **1996,** *54*, 11169-11186.

44. Kresse, G.; Furthmuller, J., Efficiency of ab-initio total energy calculations for metals and semiconductors using a plane-wave basis set. *Comput. Mater. Sci.* **1996,** *6*, 15-50.

45. Kresse, G.; Hafner, J., Ab initio molecular dynamics for liquid metals. *Physical Review B* **1993,** *47*, 558-561.

46. Kresse, G.; Hafner, J., Ab initio molecular-dynamics simulation of the liquid-metal-amorphous-semiconductor transition germanium. *Physical Review B* **1994,** *49*, 14251-14269.

47. Blöchl, P. E., Projector augmented-wave method. *Physical Review B* **1994,** *50*, 17953-17979.

48. Kresse, G.; Joubert, D., From ultrasoft pseudopotentials to the projector augmented-wave method. *Physical Review B* **1999,** *59*, 1758-1775.

49. Perdew, J. P.; Burke, K.; Ernzerhof, M., Generalized gradient approximation made simple. *Phys. Rev. Lett.* **1996,** *77*, (18), 3865-3868.

50. Perdew, J. P.; Burke, K.; Ernzerhof, M., Generalized gradient approximation made simple [Phys. Rev. Lett. 77, 3865 (1996)]. *Phys. Rev. Lett.* **1997,** *78*, (7), 1396-1396.

51. Hammer, B.; Hansen, L. B.; Nørskov, J. K., Improved adsorption energetics within density-functional theory using revised Perdew-Burke-Ernzerhof functionals. *Physical Review B* **1999,** *59*, 7413-7421.

52. Adamo, C.; Barone, V., Toward reliable density functional methods without adjustable parameters: The PBE0 model. *J. Chem. Phys.* **1999,** *110*, (13), 6158-6170.

53. Grimme, S., Semiempirical GGA-type density functional constructed with a long-range dispersion correction. *J. Comput. Chem.* **2006,** *27*, 1787-1799.

54. Grimme, S.; Antony, J.; Ehrlich, S.; Krieg, H., A consistent and accurate *ab initio* parametrization of density functional dispersion correction (DFT-D) for the 94 elements H-Pu. *J. Chem. Phys.* **2010,** *132*, 154104.

55. Alikhanov, R. A., Neutron diffraction investigation of the antiferromagnetism of the carbonates of manganese and iron. *Sov. Phys. JETP* **1959,** *36*, 1204-1208.

56. Hoover, W. G., Canonical Dynamics - Equilibrium Phase-Space Distributions. *Phys. Rev. A* **1985,** *31*, 1695-1697.

57. Rehr, J. J.; Kas, J. J.; Prange, M. P.; Sorini, A. P.; Takimoto, Y.; Vila, F. D., Ab initio theory and calculations of X-ray spectra. *C.R. Phys.* **2009,** *10*, (6), 548-559.

58. Rehr, J. J.; Kas, J. J.; Vila, F. D.; Prange, M. P.; Jorissen, K., Parameter-free calculations of x-ray spectra with FEFF9. *Phys. Chem. Chem. Phys.* **2010,** *12*, 5503-5513.

59. Newville, M., IFEFFIT: Interactive XAFS analysis and FEFF fitting. *J. Synchrotron Rad.* **2001,** *8*, 322-324.

60. Momma, K.; Izumi, F., VESTA 3 for three-dimensional visualization of crystal, volumetric and morphology data. *J. Appl. Cryst.* **2011,** *44*, 1272-1276.

61. O'Day, P. A.; Newville, M.; Neuhoff, P. S.; Sahai, N.; Carroll, S. A., X-ray absorption spectroscopy of strontium(II) coordination. *J. Colloid Interface Sci.* **2000,** *222*, 184-197.

62. Parkman, R. H.; Charnock, J. M.; Livens, F. R.; Vaughan, D. J., A study of the interaction of strontium ions in aqueous solution with the surfaces of calcite and kaolinite. *Geochim. Cosmochim. Acta* **1998,** *62*, (9), 1481-1492.

63. Finch, A. A.; Allison, N., Coordination of Sr and Mg in calcite and aragonite. *Mineral Mag.* **2007,** *71*, 539-552.

64. Singer, D. M.; Johnson, S. B.; Catalano, J. G.; Farges, F.; Brown Jr., G. E., Sequestration of Sr(II) by calcium oxalate - A batch uptake study and EXAFS analysis of model compounds and reaction products. *Geochim. Cosmochim. Acta* **2008,** *72*, 5055-5069.

65. Wallace, S. H.; Shaw, S.; Morris, K.; Small, J. S.; Burke, I. T., Alteration of sediments by hyperalkaline K-rich cement leachate: Implications for strontium adsorption and incorporation. *Environ. Sci. Technol.* **2013,** *47*, 3694-3700.

66. Singer, J. W.; Yazaydin, A. O.; Kirkpatric, R. J.; Bowers, G. M., Structure and transformation of amorphous calcium carbonate: A solid-state ^{43}Ca NMR and computational molecular dynamics investigation. *Chem. Mater.* **2012,** *24*, 1828-1836.

67. De Villiers, J. P. R., Crystal structures of aragonite, strontianite, and witherite. *Am. Miner.* **1971,** *56*, 758-767.

68. Littlewood, J. L.; Shaw, S.; Peacock, C. L.; Bots, P.; Trivedi, D.; Burke, I. T., Mechanism of enhanced strontium uptake into calcite via an amorphous calcium carbonate crystallization pathway. *Crystal Growth & Design* **2017,** *17*, 1214-1223.

69. Gräfe, M.; Singh, B.; Balasubramanian, M., Surface speciation of Cd(II) and Pb(II) on kaolinite by XAFS spectroscopy. *J. Colloid Interface Sci.* **2007,** *315*, 21-32.

70. Sun, Q.; Liu, C.; Cui, P.; Fan, T.; Zhu, M.; Alves, M. E.; Siebecker, M. G.; Sparks, D. L.; Wu, T.; Li, W.; Zhou, D.; Wang, Y., Formation of Cd precipitates on γ-Al_2O_3: Implications for Cd sequestration in the environment. *Environ. Inter.* **2019,** *126*, 234-241.

71. Khaokaew, S.; Chaney, R. L.; Landrot, G.; Ginder-Vogel, M.; Sparks, D. L., Speciation and release kinetics of cadmium in an alkaline paddy soil under various flooding periods and draining conditions. *Environ. Sci. Technol.* **2011,** *45*, 4249-4255.

72. Van Damme, A.; Degryse, F.; Smolders, E.; Sarret, G.; Dewit, J.; Swennen, R.; Manceau, A., Zinc speciation in mining and smelter contaminated overbank sediments by EXAFS spectroscopy. *Geochim. Cosmochim. Acta* **2010,** *74*, 3707-3720.

73. Jacquat, O.; Voegelin, A.; Juillot, F.; Kretzschmar, R., Changes in Zn speciation during soil formation from Zn-rich limestones. *Geochim. Cosmochim. Acta* **2009,** *73*, 5554-5571.

74. Cheng, L.; Sturchio, N. C.; Bedzyk, M. J., Local structure of Co^{2+} incorporated at the calcite surface: An x-ray standing wave and SEXAFS study. *Physical Review B* **2000,** *61*, (7), 4877-4883.

TOC GRAPHIC